Chapter 6

Magnetic Resonance (MR)-transverse relaxivity in interacting ensembles of anisotropic nanosystems

6.1 INTRODUCTION

The ensemble of anisotropic MNPs is a smart approach to achieve enhanced longitudinal (r_1)/transverse (r_2) Magnetic Resonance (MR)-relaxivity [1,2]. MNPs yield a local field that agitates nuclear relaxation and as a result, shortens proton relaxation. This further results in enhanced contrast nature of MRI images [3−5]. However, the dynamic interaction of magnet as well as water protons gives relaxation modulation. Indeed, MNPs arrangement in an ensemble can further alter the efficiency of MRI contrast [6,7]. The morphological arrangement of MNPs modulates the magnetization, due to tailored exchange/dipolar strength, with modified surface effects. However, the morphology of MNPs controls magnetic switching nature, due to enhanced shape anisotropy [8,9].

Generally, quantum-mechanical outer-sphere diffusion theories give a detailed idea of r_2 enhancement in MR relaxivity for SPM systems, with the aid of motional averaging regime (MAR) condition [10−12]. However, r_2 is dependent on magnetization, structural correlation as well as water diffusivity. As SPM has negligible moment, consideration of more inherent magnetic parameters reliance is required in order to explore r_2 enhancement [13−15]. The complexity residing in structural geometry results in a deeper investigation of r_2. The consideration of anisotropic MNPs of single-domain retains multiple magnetic poles that make the energy domain more complicated as compared to isotropic nanosystems. The shape of MNPs gives an important role, due to field coupling among MNPs [16−21]. In addition, the spin orientation and distance among MNPs as well as

K. Konwar, et al. Structure-Correlated Magnetic Resonance Transverse Relaxivity Enhancement in Superparamagnetic Ensembles with Complex Anisotropy Landscape, *Langmuir,* 38:11087−11098, 2022.

respective spin motion in their ensembles modify either proton-electron interaction or proton-proton interaction, that can monitor r_2. Therefore, consideration of an in-detail explanation of structure-regulated dynamic responses as well as MR-transverse enhancement in different geometric ensembles of anisotropic MNPs is needed.

Herein this Chapter, MR-transverse relaxivity is evaluated by considering the different patterns of MNPs in respective ensembles: Compact Ensemble of Isotropic Zinc Ferrite (CEIZF), Compact Ensemble of Anisotropic-Isotropic Zinc Ferrite (CEAIZF), and Core-Shell Ensemble Zinc Ferrite (CSEZF). Two other morphologies are investigated: Compact Ensemble of Zinc Ferrite (CEZF) and Hollow Core Ensemble Zinc Ferrite (HCEZF). The related structural correlation and dynamic magnetic behaviour of the other two systems are performed in Chapter 2. Here, the nature of the anisotropy landscape as well as easy axes arrangement is correlated with MR-relaxivity efficacy. However, the structural correlation of the ensemble with the varied organization of MNPs is explored with SAXS and SANS experiments. The anisotropy energy landscape variation having varied easy axes alignment provides spin-spin relaxation modification. An enhanced r_2 is addressed in the MR-relaxivity mechanism. A relation of r_2/r_1 enhancement with the aid of organization pattern of MNPs, and dynamic magnetic nature is drawn in this chapter.

6.2 EXPERIMENTAL DETAILS

6.2.1 Synthesis of MNPs

The development procedure of ensembles is consistent with Chapter 2 with a slight modification [22] as reaction periods are varied as 1 h for CEIZF, 8 h for CEAIZF, CEZF for 12 h, and 18 h for CSEZF. The HEK-293 cell is achieved from National Center for Cell Science (Pune, India) and DMEM (Dulbecco's Modified Eagle Medium) as well as FBS (Fetal Bovine Serum) are attained from Life Technologies, USA. MTT (3-(4,5-dimethylthiazolyl-2)-2,5-diphenyltetrazolium

bromide) is acquired from Sigma−Aldrich, USA. The rest of the instrumental details and characterization techniques are similar to previous chapter 5.

6.3 RESULTS AND DISCUSSIONS

6.3.1 Microstructural study

The HRTEM images are performed for morphological confirmation, as depicted in Figures 6.1(a-i). In the case of 1 h reaction time, a spherical ensemble of isotropic MNPs is formed as displayed in Figures 6.1(a-c). In this reaction time, spherical MNPs are forming with isotropic ensembles of radius ~120 nm following the Ostwald ripening mechanism for growth. At 8 h reaction time, few elongated MNPs will form on the surface as depicted in Figures 6.1(d-f). For 12 h reaction time, compact ensembles of anisotropic MNPs are achieved, as described in Figures 6.1(g-i). With an increase in time to 18 h, the growth of nanorods having a diameter of 4 nm, is found with a core-shell morphology, as seen in Figures 6.1(j-l). For 21 h, a hollow ensemble is seen as depicted in Figure 6.1(m-o). Moreover, FESEM is seen in Figure 6.2., which further confirms development of ensembles with varied organization of MNPs. Figure 6.2(a) shows an isotropic ensemble having isotropic MNPs. The development of anisotropic MNPs in CEAIZF is depicted in Figure 6.2(b). Figure 6.2(c) also confirms the development of a compact ensemble. The existence of core-shell structure in CSEZF is ensured in Figure 6.2(d), which is depicted by yellow arrows. Moreover, the development of a hollow interior in HCEZF is ensured in Figure 6.2(e). The different morphology is achieved by the "Inside-out Ostwald Ripening" mechanism, with oriented attachment, which results in the development of anisotropic MNPs.

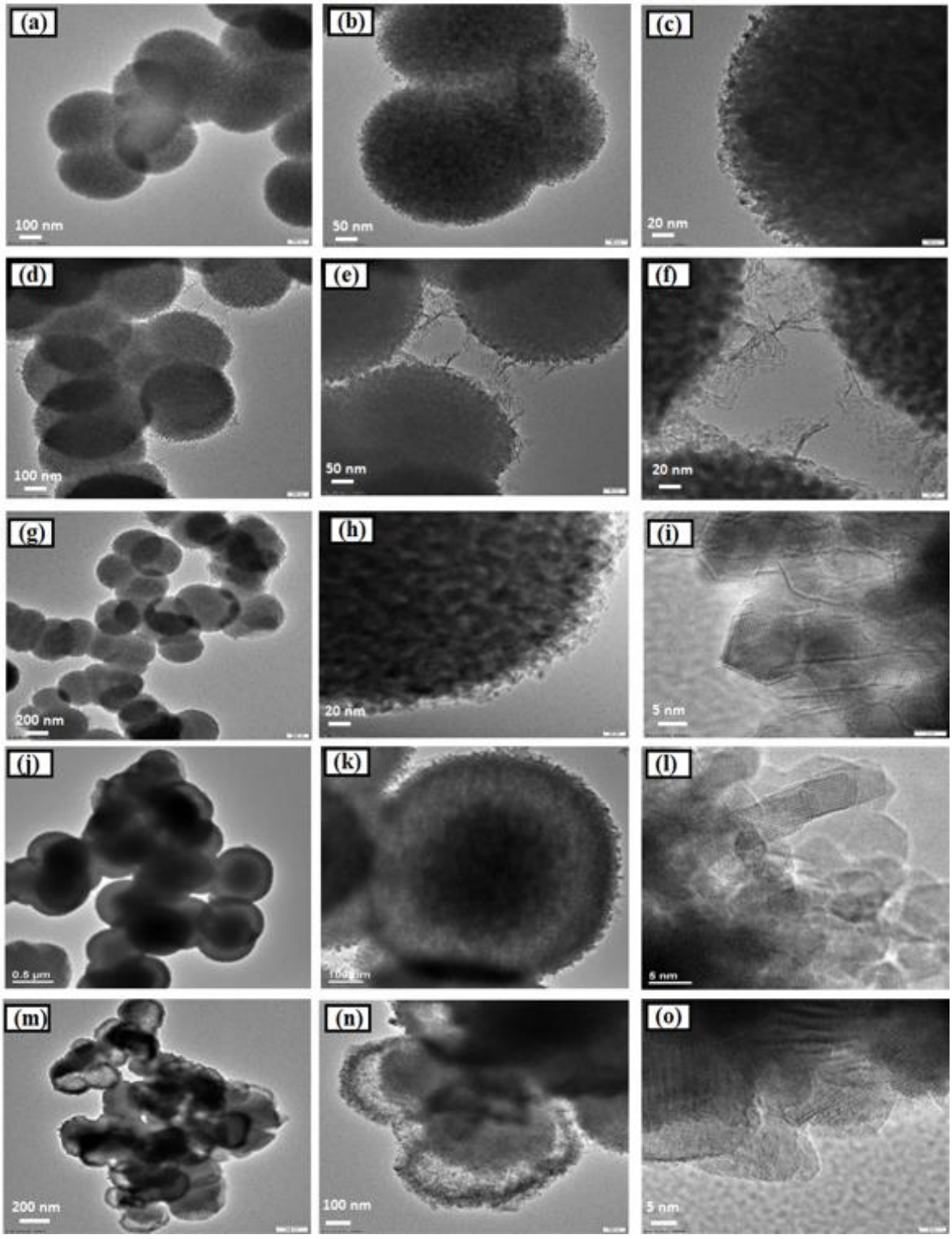

Figure 6.1: TEM images of (a, b, c) CEIZF, (d, e, f) CEAIZF (g, h, i) CEZF; (j, k, l) CSEZF, (m, n, o) HCEZF.

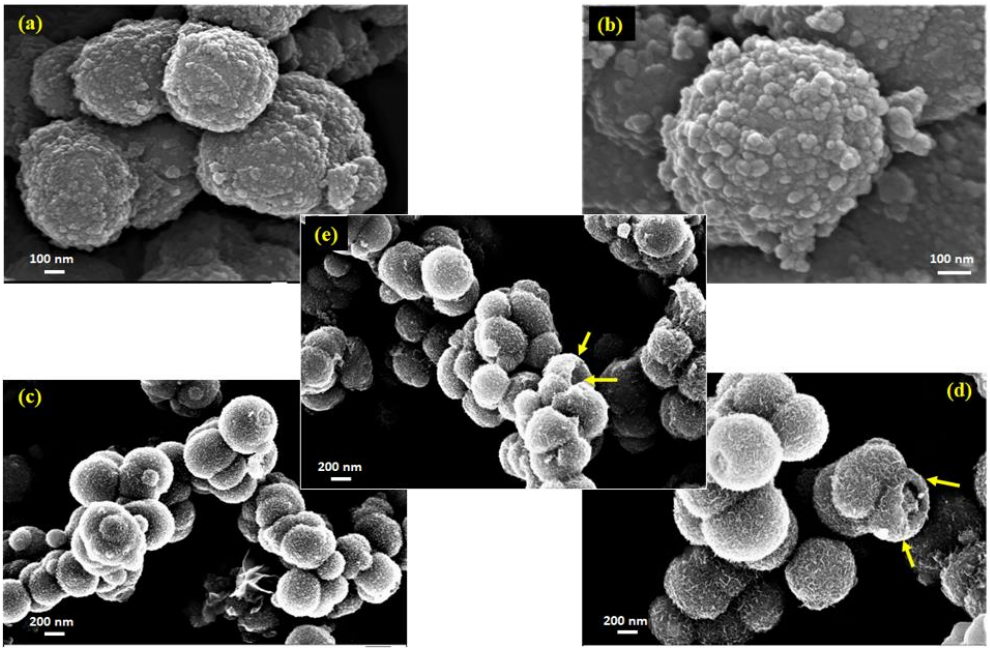

Figure 6.2: FESEM images of (a) CEIZF, (b) CEAIZF, (c) CEZF, (d) CSEZF, (e) HCEZF.

Figures 6.3(a-c) predict SAXS and SANS profiles, which explain two patterns of hierarchy in the systems. The detailed structural information for CEZF and HCEZF is executed in Chapter 2. The achieved log-log curve of the SAXS profile of CEIZF following spherical model for form factor in primary MNPs as well as SANS profile fits through similar spherical form factor in case of secondary ensemble. In CEAIZF, cylindrical and spherical form factors are considered for log-log profile fitting by various contributions. Moreover, SANS profile fits with spherical form factor. Still, CSEZF fits accurately considering the cylindrical form factor as well as the structure factor model of the sticky hard sphere (SHS) in the SAXS profile. The scattering confirms the existence of SHS interaction. The distribution function of log-norm form is taken for SAXS and MSANS profiles fitting [22]. The intensity profile fitting supports HRTEM images. The obtained parameters are depicted in Tables 6.1 and 6.2, to achieve polydispersity index (σ), MNPs diameter (D) in nm, and MNPs length (L) in nm.

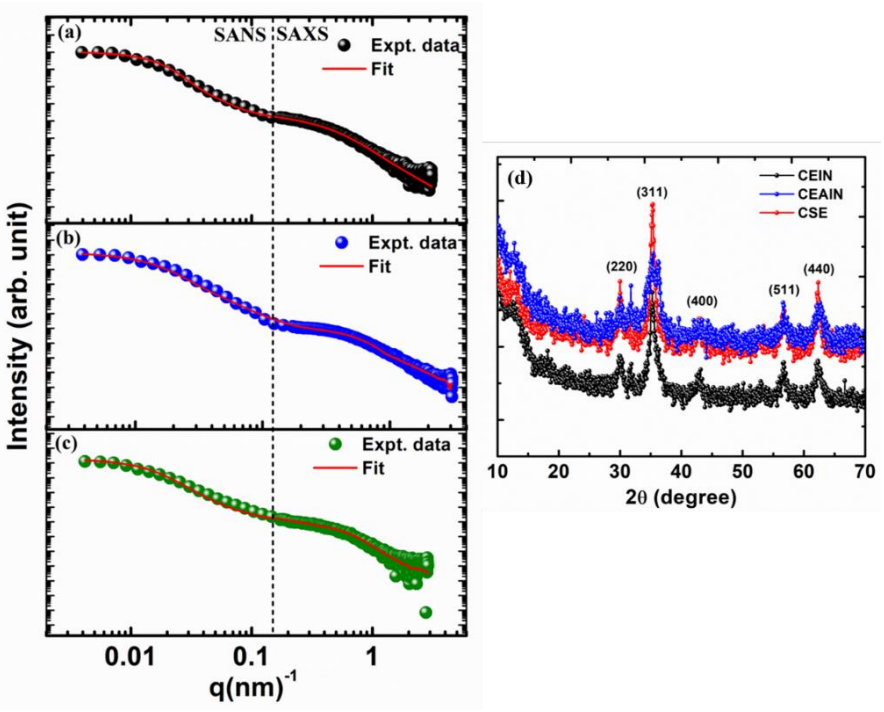

Figure 6.3: SAXS and MSANS fitting (a) CEIZF, (b) CEAIZF, and (c) CSEZF; (d) X-ray Diffraction curves.

Table 6.1. Fitting of SAXS profile for primary MNPs.

System	Contribution 1				Contribution 2				Contribution 3		
Name	Shape	σ	D	L	shape	σ	D	L	Type	τ	fp
CEIZF	Sphere	.18	5.0	---	Sphere	0.20	2.6	---	SHS	-	-
CEAIZF	Sphere	.27	7.0	---	Long Cylinder	0.22	6	15	SHS	0.1	0.1
CSEZF	Long Cylinder	.27	6.0	22	Long Cylinder	0.08	6	4	SHS	0.24	0.1

Table 6.2. Fitting values from the SANS profile for ensembles.

System	Secondary system from MSANS fitting		
Name	Shape	σ	D in nm
CEIZF	Spherical	0.280	190.0
CEAIZF	Spherical	0.360	204.0
CSEZF	Spherical	0.380	180.0

The achieved results ensure the development of the $ZnFe_2O_4$ phase by XRD study, as displayed in Figure 6.3(d). The low crystal defects and higher crystallinity are confirmed from XRD plots as per the JCPDS Card No. 82-1042, similar to Chapter 2. With an enhanced reaction period from 1 to 18 h, crystallinity is enhanced as the nucleation period is higher. As a result, CSEZF shows prominent and sharp peaks. The developed systems are considered for further inherent magnetic nature investigations [22−25], and in-detail magnetic analysis is performed.

6.3.2 Direct Current Magnetization Study

The magnetic nature in the considered system is performed by considering both field and temperature relying magnetization. The dynamic magnetic analysis for systems CEZF and HCEZF is given in Chapter 2. The M−H curve is executed at 300 K, 150 K, 30 K, and 5 K, as depicted in Figure 6.4. The systems are exhibiting room temperature SPM state with a narrow hysteresis loop. The coercivity is calculated as 37.9 Oe for CEIZF, 37.6 Oe for CEAIZF, and 9.5 Oe for CSEZF systems. CSEZF shows the lowest coercivity value. LAS fitting is evaluated as provided in equation 2.7 of chapter 2, as depicted in Figure 6.5. K values for

CEIZF are achieved as 6.40 × 10^3 erg cm^{-3} for 300 K, 1.50 × 10^4 erg cm^{-3} for 150 K, 3.20 × 10^4 erg cm^{-3} for 30 K, and 4.90 × 10^4 erg cm^{-3} for 5 K. For CEAIZF, K values are 1.10 × 10^4 erg cm^{-3} at 300 K, 2.20 × 10^4 erg cm^{-3} for 150 K, 3.50 × 10^4 erg cm^{-3} for 30 K, and 5.80 × 10^4 erg cm^{-3} for 5 K. For CSE, K values 5.50 × 10^3 erg cm^{-3} for 300 K, 8.90 × 10^3 erg cm^{-3} for 150 K, 2.40 × 10^4 erg cm^{-3} for 30 K, and 5.40 × 10^4 erg cm^{-3} for 5 K. The values show a temperature-dependent trend in magneto-crystalline anisotropy. The high anisotropy in energy landscape is ensured.

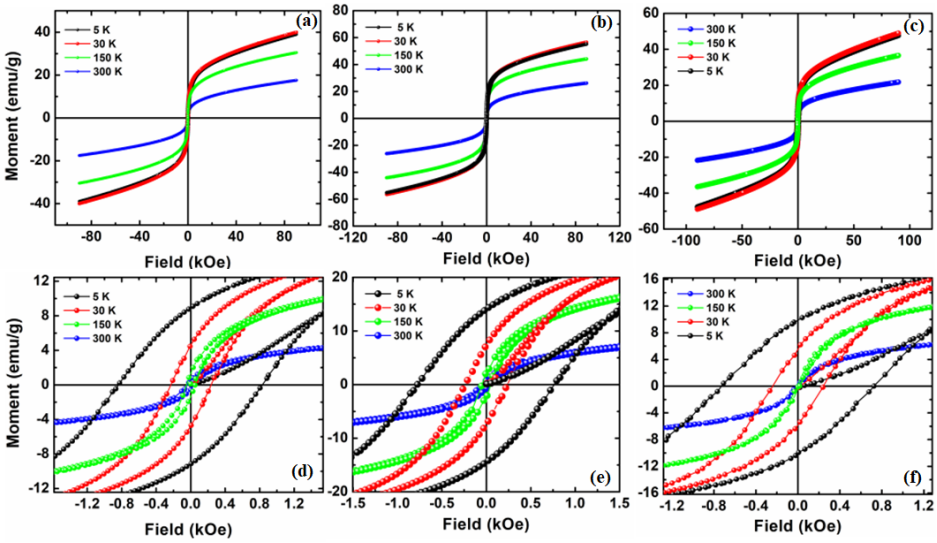

Figure 6.4: Field relying magnetization: (a) CEIZF, (b) CEAIZF, (c) CSEZF; Zoomed hysteresis pattern view: (d) CEINZF, (e) CEAINZF, (f) CSEZF.

CSEZF reflects enhanced anisotropy, compared to CEIZF and CEAIZF. It confirms the complex anisotropic energy landscape in CSEZF. In addition, reduced remanence is evaluated and achieved as 0.42 emu/g for CEIZF, 0.38 emu/g for CEAIZF, and 0.32 emu/g for CSEZF, confirming dominance of single-domain MNPs of uniaxial anisotropy [22]. The trend of magnetization with temperature is depicted with ZFC and FC magnetization studies considering fields of 100 Oe and 1000 Oe, as depicted in Figure 6.6. The observed bifurcation below room temperature ensures existence of SPM state [23]. The peak in ZFC plot gives blocking temperature of SPM state at that temperature. A possible shift from SPM state to blocked state is found at temperature 104 K and 40 K at field

100 Oe and field 1000 Oe for CEIZF; at 98 K and 38 K at 100 Oe and 1000 Oe for CEAIZF; and at 122 K at a field of 100 Oe and 42 K at 1000 Oe for CSEZF.

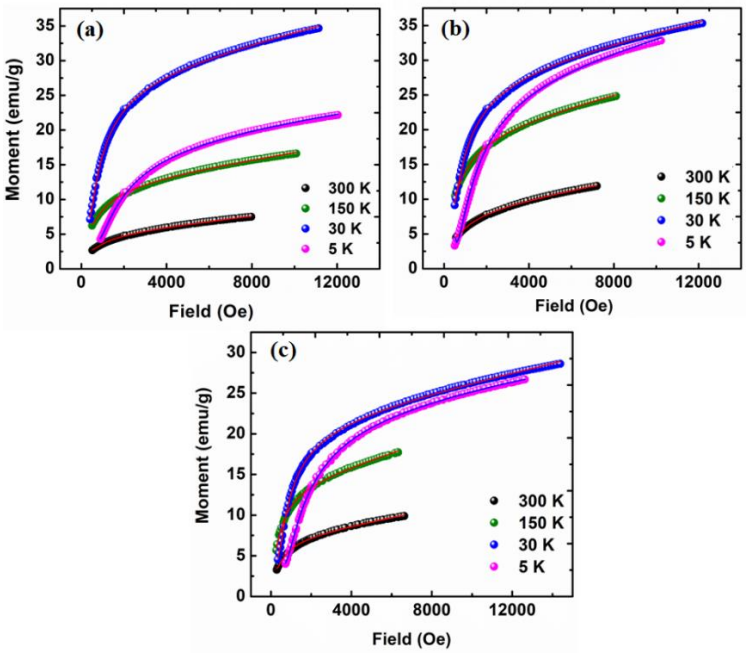

Figure 6.5: LAS fitting at temperatures 300 K, 150 K, 30 K, 5 K: (a) CEIZF, (b) CEAIZF, (c) CSEZF.

If applied field is increased, a trend of moment reduction occurs, confirming existence of MNPs interaction. In addition, the decreasing magnetization value in the blocked state might be due to spin frustration. Curie−Weiss (CW) law is considered at 1000 Oe and the fitting is depicted in the inset of Figure 6.6 as per equation 2.8 of chapter 2. The fitting values are found as, Curie temperature, θ_{CW} = 90 K and Curie constant, C = 0.0850 g cm^{-3} K for CEIZF; θ_{CW} = 115 K and C = 0.13360 g cm^{-3} K for CEAIZF; and θ_{CW} = 80 K, C = 0.120 g cm^{-3} K for CSEZF. The positive θ_{CW} ensures ferromagnetic ordering [22, 23]. The respective effective magnetic moment (μ_{eff}) is calculated as μ_{eff} = 0.82 μ_B for CEIZF, μ_{eff} = 1.03 μ_B for CEAIZF, and μ_{eff} = 0.98 μ_B for CSEZF. The existence of anisotropic MNPs results in a broadening in T_B with a shift to a higher temperature range. However, core-shell arrangement can enhance shape anisotropy, compared to other ensembles. The enhancement in shape anisotropy can lower magnetic coercivity value

because of the complexity of the energy landscape. Hence, structure-correlated collective magnetic characteristics can be explained by varying easy axes patterns which are discussed.

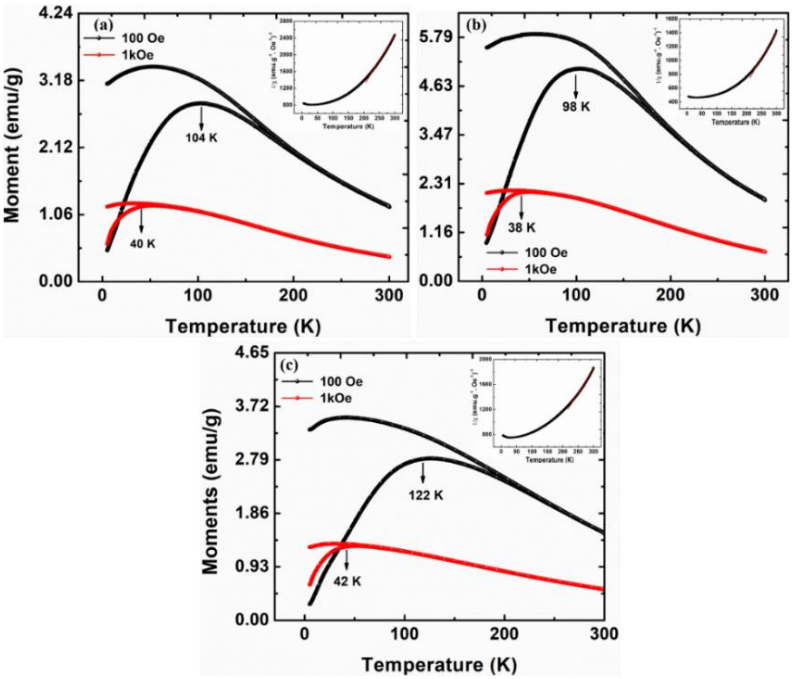

Figure 6.6: Temperature-relying magnetization: (a) CEIZF, (b) CEAIZF, (c) CSEZF ((The blocking temperature is shown with a downward arrow in both the Zero Field Cooling (ZFC) curve); Inset is given for CW-law fitting: (a) CEIZF, (b) CEAIZF, and (c) CSEZF.

The alignment of easy exes is evaluated with FC magnetization at low temperatures, similar to Chapter 2. $\frac{M_{FC}^{align}}{M_{FC}}$ provides the alignment information of easy axes as explained in equation 2.17 of chapter 2. The system CEIZF is considered a system having arbitrarily oriented easy axes and easy axes arrangement is considered [22]. $\frac{M_{FC}^{align}}{M_{FC}}$ gives 1.110 for CEAIZF and 1.230 for CSEZF. The achieved higher value than unity in CEAIZF signifies possibility of partial alignment in easy axes. Moreover, CSEZF shows more alignment in spins. Such modulation in easy axes configuration of MNPs can modulate the spin dynamics.

6.3.3 Zeta Potential and Cytotoxicity Analysis

In Figure 6.7(a), zeta potential curves are shown for CEIZF, CEAIZF, CEZF, CSEZF, and HCEZF with the aid of phosphate-buffered saline (PBS) solvent. The achieved zeta potential is 23.24 mV for CEIZF, 38.05 mV for CEAIZF, 38.05 mV for CEZF, 38.61 mV for CSEZF, and 17.67 mV for HCEZF. The steric stabilization is confirmed by the attained values. The observed morphological non-uniformity gives a higher hydrodynamic size having a high polydispersity index as given in Appendix Figure A.3. However, *in vitro* cytotoxicity of agarose-stabilized MNPs is performed for varied metal concentrations through MTT assay with the aid of HEK-293 cell line, as depicted in Figure 6.7(b). It is observed that the SPM MNPs with 24 h incubation provide acceptable cell viability till 0.5 mM metal concentrations. However, cell viability is slightly lower than 60% but higher than 55 % at 1 mM. The decrease in viability of the cell was seen at 0.001mM and it again increased at 0.5 mM. The estimation for cell viability was done using MTT assay which involves washing and media removal steps from the treatment stage to MTT addition. As such, this trend is observed due to minor washing inconsistency and it doesn't interfere with the conclusions made from this data. This is one of the minor drawbacks of using MTT assay as it involves washing and media removal to dissolve the formazan crystals in a dissolving solution. As seen in the results, the system shows appreciable viability in all these concentrations. The dip at 1 mM is due to the decline in the viability of cells upon treatment with the system. Stricter and careful washing protocols can be followed to have a consistent trend.

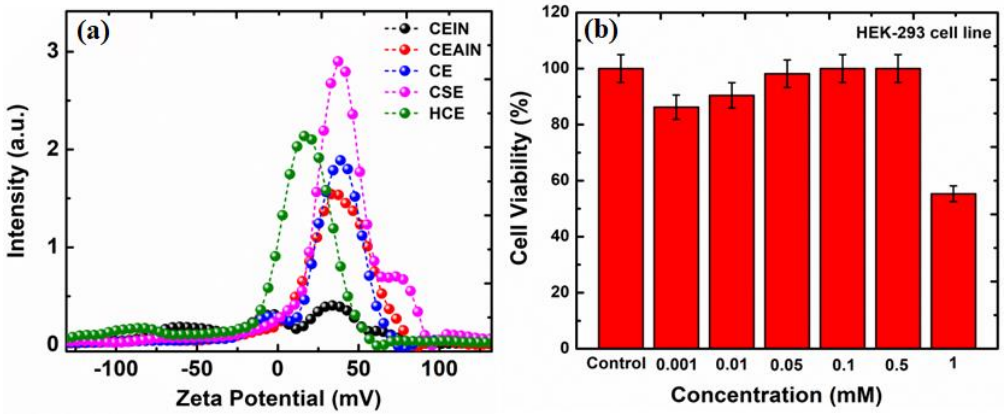

Figure 6.7: (a) Zeta potential curves in PBS solution, (b) MTT assay for cytotoxicity analysis of HCEZF considering HEK-293.

6.3.4 MR-relaxivity

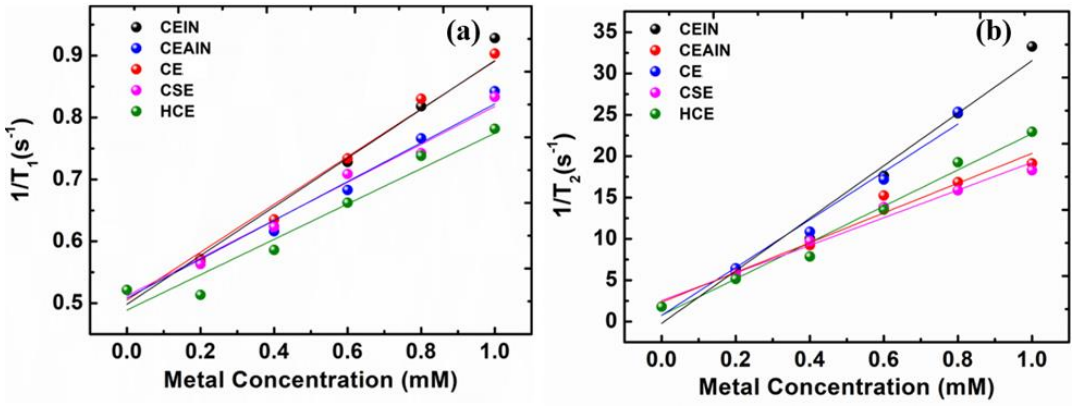

Figure 6.8: (a) r_1 plot at various metal concentrations for CEIZF, CEAIZF, CEZF, CSEZF, HCEZF; (b) r_2 at various metal concentrations for (b) CEIZF, CEAIZF, CEZF, CSEZF, and HCEZF. The error bars in data present standard deviation in experimental data.

For MR-relaxivity study, the ensembles with varied arrangements are considered. The fitting procedure of transverse and longitudinal relaxation period is similar to Chapter 5. For the MR-relaxivity study, metal concentration variation with five Zinc ferrite MNPs concentrations dispersed in agarose is considered with 0.20 mM, 0.40 mM, 0.60 mM, 0.80 mM and 1.0 mM respectively. The curves after proper fitting for each concentration are explored in Figure 6.8(a,

b). The longitudinal relaxivity is found as 0.410 s^{-1} mM^{-1} for CEIZF, 0.350 s^{-1} mM^{-1} for CEAIZF, 0.390 s^{-1} mM^{-1} for CEZF, 0.310 s^{-1} mM^{-1} for CSEZF, and 0.280 s^{-1} mM^{-1} for HCEZF at 3 T.

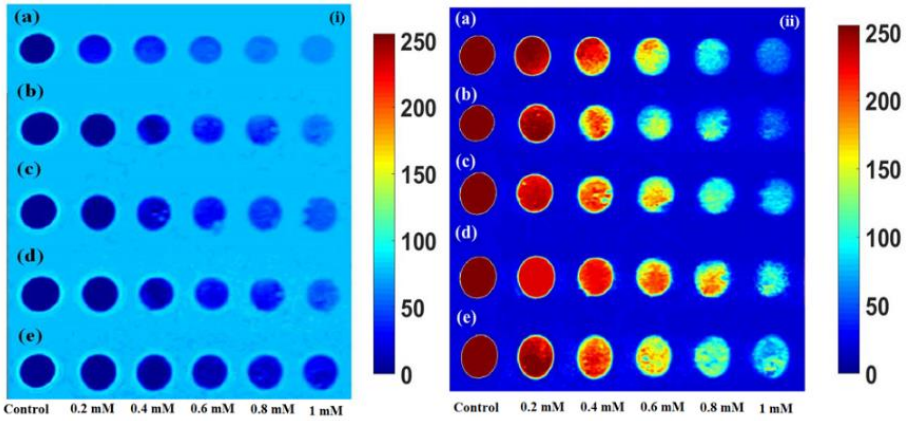

Figure 6.9: Phantom images for (i) Longitudinal relaxation T_1: (a) CEIZF, (b) CEAIZF, (c) CEZF, (d) CSEZF, (e) HCEZF; (ii) Transverse relaxation T_2: (a) CEIZF, (b) CEAIZF, (c) CEZF, (d) CSEZF, and (e) HCEZF.

Similarly, the transverse relaxation rate is executed, following a similar procedure to Chapter 5. After fitting, r_2 is achieved as 31.80 s^{-1} mM^{-1} for CEIZF, 17.0 s^{-1} mM^{-1} for CEAIZF, 28.90 s^{-1} mM^{-1} for CEZF, 16.70 s^{-1} mM^{-1} for CSEZF, and 21.90 s^{-1} mM^{-1} for HCEZF for 3 T. A diamagnetic contribution is observed ensuring inhomogeneous energy barriers dominance in the systems [33, 34]. However, the relaxation trend in the phantom image is shown in Figure 6.9, which is acquired with the aid of Siemens syngo MMWP VE36A software. The colour contrast is described with enhancement in metal concentrations and an improvement in contrast is shown in Figure 6.9(i) and a migration of light contrast is depicted from left to right in case of longitudinal relaxation. For transverse relaxation, light to dark trend in contrast is seen confirming a better contrast efficacy, as depicted in Figure 6.9(ii). The phantom image colour bar provides an idea of colour contrast. Such nature relies on the overall magnetic nature of the material [25]. The dominance of spin relaxation nature is executed by calculating $\frac{r_2}{r_1}$, which results in a value lower than 3 for longitudinal

relaxation, and a value between 3 to 10, for dual-mode longitudinal and transverse relaxation nature. A value higher than 10, results because of transverse relaxation. Herein, $\frac{r_2}{r_1}$ is achieved as 77.5 for CEIZF, 49.1 for CEAIZF, 74.2 for CEZF, 53.6 for CSEZF, and 78.4 for HCEZF, confirming MR-transverse behaviour [31, 32].

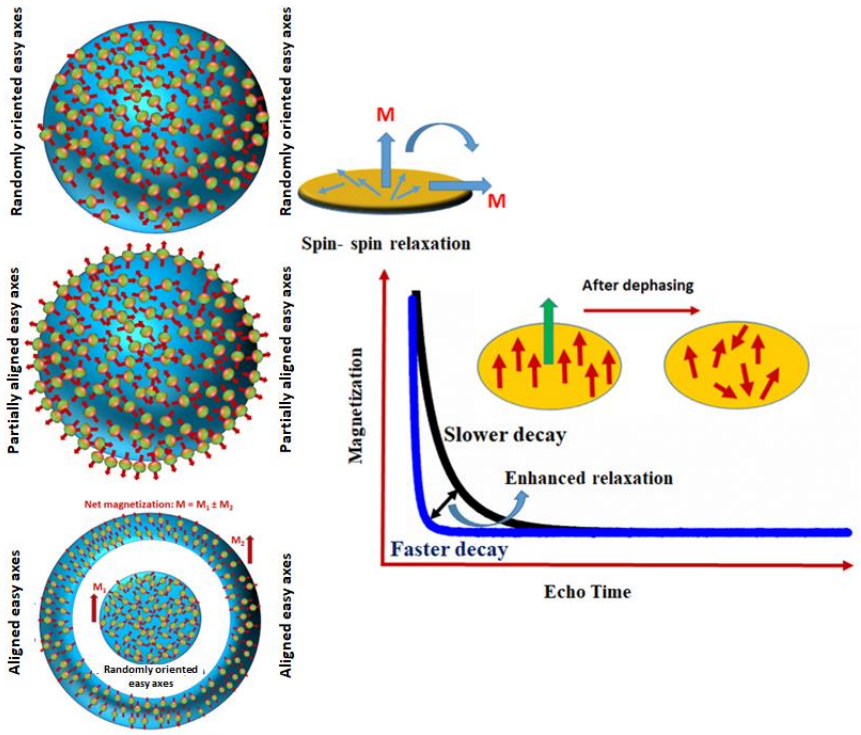

Figure 6.10: A Schematic presentation for varied easy axes in a complex anisotropy landscape and respective faster transverse relaxation trend.

MR-transverse relaxivity relies on the square of magnetization as well as the magnetic core. In quantum-mechanical outer-sphere diffusion theory, magnetic moment dependency on transverse relaxation follows a relation in the MAR region as [34, 35]:

$$R_2 = \frac{1}{T_2} = \frac{256\,\pi^2\gamma^2}{405}\, M_S^2 V^* \frac{r^2}{D(1+ L/r)} \qquad (6.1)$$

In which, M_s gives magnetization per unit volume of MNPs, γ gives proton gyromagnetic ratio value, V* gives volume fraction, and D is water molecule diffusivity with surface coating thickness of L and core-radius of r. In the case of SPM MNPs, structure-regulated anisotropy as well as the shape and organization of MNPs perturb water proton phase coherency, because of the modified magnetic anisotropy landscape. To understand of inherent relation of structure-regulated relaxivity, a detailed understanding of inherent magnetic dependency is required to consider. In such a case, the realization of the collective magnetic nature of transverse MR-relaxivity modulation is important by considering various spin organizations and easy axes arrangement in their ensembles, which is depicted in Figure 6.10. For CEIZF, shape anisotropy is reduced and hence a less-complicated dynamics is addressed. In CEAIZF, wherein both isotropic and anisotropic MNPs are there, shape anisotropy is enhanced. The pattern of easy axes gives efficient magnetic inhomogeneity. In CSEZF, spins in the shell are present maintaining prominent spacing with an alignment following a net magnetization addressed as M_1 as depicted in Figure 6.10. In the aligned single domain MNPs having significant space aids easy diffusivity for water protons inside respective ensemble. The space between core and shell further gives enhancement diffusion of water protons. The spins of core, which are arbitrarily oriented with dense populations, provide closer proximity in spins. The net magnetization of randomly oriented moments is addressed as M_2. In such an arrangement with enhanced magneto-crystalline anisotropy, a net magnetization of ($M_1 \pm M_2$) is considered. The anisotropic energy contribution can be considered to understand the non-equilibrium decay of moments and a modified expression is hypothesized as follows:

$$\frac{1}{T_2} = \frac{256\,\pi^2\gamma^2}{405}\, M_S^2 V^* \,\frac{r^2}{D(1+L/r)}\,\frac{8}{105}\,\frac{K^2}{M_S^2\,\mu^2}\,\{1 + \alpha(3\cos^2\beta - 1)\} \qquad (6.2)$$

Herein, magneto-crystalline anisotropy energy per field, $\frac{K^2}{M_S^2\ \mu^2}$, is considered to explain MR-transverse relaxation. This term is considered from the B/H^2 term of the LAS model, in which B can be represented as: $\frac{K^2}{M_S^2\ \mu^2}$. H is taken as the unit field for numerical simplification. In order to maintain the dimensional unity, the unit of applied field should be considered. However, K is the anisotropy constant with the permeability of μ as well as saturation magnetization per unit of MNPs volume, M_s. To address the easy axes direction, the term $\{1 + \alpha(3\cos^2\beta - 1)\}$ is introduced in equation 6.2 where α is degree of aligned easy axes and cos β provides an angle between the imposed field and the respective easy axis. The existence of a demagnetizing field can modulate the relaxation period of MR-relaxivity. The role of easy axes orientation as well as anisotropy energy in MAR equation is essential to consider. The aforementioned proposed hypothesis gives inherent detail of transverse relaxation enhancement in SPM complex ensembles. The existence of aligned as well as random easy axes provide competing anisotropy landscape and can impact the faster transverse relaxation in the magnetization trend than that of the longitudinal relaxation trend. Hence, MR-transverse relaxivity can be attained by considering other dynamic magnetic responses such as anisotropy landscape and easy axis orientation in complex superparamagnetic nano-structures. The ensembles show steric stability, promising cell viability, and significant efficacy in MR-transverse relaxivity, further supporting as a promising candidate for MRI.

6.4 CONCLUDING REMARKS

A correlation of structure-modulated MR-relaxivity is addressed in complex ensembles having different arrangements of MNPs. The thermal-energy-dependent magneto-crystalline anisotropy is found to be dominating the MR-transverse relaxation mechanism, with enhanced r_2/r_1. In CEIZF, randomly distributed easy axes having higher anisotropy energy provide enhancement in MR-relaxivity efficacy. In HCEZF, partially aligned easy axes having lower

anisotropy results in enhanced MR-transverse efficacy. Low r_2 in CSEZF with high anisotropy energy as well as presence of aligned and random easy axes is evident. A correlation of dynamic magnetic responses on r_2 enhancement is established by considering a varied geometric arrangement of MNPs with easy axes alignment.

References:

(1) Saikia, K., Bhattacharya, K., Sen, D., Kaushik, S. D., Biswas, J., Lodha, S., Gogoi, B., Buragohain, A. K., Kockenberger, W. and Deb, P. Solvent evaporation driven entrapment of magnetic nanoparticles in mesoporous frame for designing a highly efficient MRI contrast probe. *Applied Surface Science,* 464:567, 2019.

(2) Deng, H., Li, X., Peng, Q., Wang, X., Chen, J. and Li, Y. Monodisperse Magnetic Single-Crystal Ferrite Microspheres. *Angewandte Chemie,* 44:2782, 2005.

(3) Park, J., Joo, J., Kwon, S. G., Jang, Y. and Hyeon, T. Synthesis of Monodisperse Spherical Nanocrystals. *Angewandte Chemie,* 46:4630, 2007.

(4) Wilhelm, M. J., Ong, H. H., Wehrli, S. L., Li, C., Tsai, P.-H., Hackney, D. B. and Wehrli, F. W. Direct magnetic resonance detection of myelin and prospects for quantitative imaging of myelin density. *Proceedings of the National Academy of Sciences U.S.A.,* 109:9605, 2012.

(5) Degen, C. L., Poggio, M., Mamin, H. J., Rettner, C. T. and Rugar, D. Nanoscale magnetic resonance imaging. *Proceedings of the National Academy of Sciences U.S.A.,* 106:1313, 2009.

(6) Pervushin, K., Riek, R., Wider, G. and Wuthrich, K. Attenuated T_2 relaxation by mutual cancellation of dipole−dipole coupling and chemical shift anisotropy indicates an avenue to NMR structures of very large biological macromolecules in solution. *Proceedings of the National Academy of Sciences U.S.A.,* 94:12366, 1997.

(7) Taboada, E., Rodríguez, E., Roig, A., Oró, J., Roch, A. and Muller, R. N. Relaxometric and Magnetic Characterization of Ultrasmall Iron Oxide Nanoparticles with High Magnetization. Evaluation as Potential T_1 Magnetic Resonance Imaging Contrast Agents for Molecular Imaging. *Langmuir*, 23:4583, 2007.

(8) Jordan, S. P., Hu, S., Rozada, I., McGivney, D. F., Boyacioğlu, R., Jacob, D. C., Huang, S.; Beverland, M.; Katzgraber, H. G., Troyer, M., Griswold, M. A. and Ma, D. Automated design of pulse sequences for magnetic resonance fingerprinting using physics-inspired optimization. *Proceedings of the National Academy of Sciences U.S.A.,* 118:e2020516118, 2021.

(9) Szczęch, M., Łopuszyńska, N., Tomal, W., Jasiński, K., Węglarz, W. P., Warszyński, P. and Szczepanowicz, K. Nafion-Based Nanocarriers for Fluorine Magnetic Resonance Imaging. *Langmuir,* 36:9534, 2020.

(10) Xing, H., Zhang, S., Bu, W., Zheng, X., Wang, L., Xiao, Q., Ni, D., Zhang, J., Zhou, L., and Peng, W. Ultrasmall NaGdF 4 Nanodots for Efficient MR Angiography and Atherosclerotic Plaque Imaging. *Advanced Materials,* 26:3867, 2014.

(11) Chen, F., Bu, W., Zhang, S., Liu, X., Liu, J., Xing, H., Xiao, Q., Zhou, L., Peng, W., Wang, L. and Shi, J. Positive and Negative Lattice Shielding Effects Co-existing in Gd (III) Ion Doped Bifunctional Upconversion Nanoprobes. *Advanced Functional Materials,* 21:4285, 2011.

(12) Zhou, Z., Huang, D., Bao, J., Chen, Q., Liu, G., Chen, Z., Chen, X. and Gao, J. A Synergistically Enhanced T_1−T_2 Dual-Modal Contrast Agent. *Advanced Materials,* 24:6223, 2012.

(13) Kiselev, V. G.; Novikov, D. S. Transverse NMR Relaxation as a Probe of Mesoscopic Structure. *Physical Review Letters,* 89:278101, 2002.

(14) Stoller, S. D., Happer, W. and Dyson, F. J. Transverse spin relaxation in inhomogeneous magnetic fields. *Physical Review A,* 44:7459, 1991.

(15) Alghamdi, N. A., Hankiewicz, J. H., Anderson, N. R., Stupic, K. F., Camley, R. E., Przybylski, M., Zukrowski, J. and Celinski, Z. Development of Ferrite-Based Temperature Sensors for Magnetic Resonance Imaging: A Study of $Cu_{1-x}Zn_xFe_2O_4$. *Physical Review Applied,* 9:054030, 2018.

(16) Thapa, B., Diaz-Diestra, D., Badillo-Diaz, D., Sharma, R. K., Dasari, K., Kumari, S., Holcomb, M. B., Beltran-Huarac, J., Weiner, B. R. and Morell, G. Controlling the transverse proton relaxivity of magnetic graphene oxide. *Scientific Reports,* 9:5633, 2019.

(17) Muller, R., Gillis, P., Moiny, F. and Roch, A. Transverse relaxivity of particulate MRI contrast media: from theories to experiments. *Magnetic Resonance in Medicine,* 22:178, 1991.

(18) Lee, M. K., Clay, N. E., Ko, E., Smith, C. E., Chen, L., Cho, N., Sung, H.-J., DiPietro, L., Lee, J. and Kong, H. Spatial Organization of Superparamagnetic Iron Oxide Nanoparticles in/on Nano/Micro-Sized Carriers Modulates the Magnetic Resonance Signal. *Langmuir,* 34 (50):15276, 2018.

(19) Ibanez-Azpiroz, J., dos Santos Dias, M., Blugel, S. and Lounis, S. Longitudinal and transverse spin relaxation times of magnetic single adatoms: An ab initio analysis. *Physical Review B,* 96:144410, 2017.

(20) Richards, P. M. Relaxation of Longitudinal and Transverse Components of Nuclear Magnetization in Liquids. *Physical Review*, 132:27, 1963.

(21) Albash, T. and Marshall, J. Comparing relaxation mechanisms in quantum and classical transverse-field annealing. *Physical Review Applied,* 15:014029, 2021.

(22) Konwar, K., Kaushik, S. D., Sen, D. and Deb, P. Dynamic spin freezing and magnetic memory effect in ensembles of interacting anisotropic magnetic nanoparticles. *Physical Review B*, 102:174449, 2020.

(23) Bhattacharya, K., Dupuis, V., Le Roy, D. and Deb, P. Progressive freezing of interacting spins in isolated finite magnetic ensembles. *Journal of Physics: Condensed Matter,* 29:045002, 2017.

(24) Saikia, K., Sarma, D. D. and Deb, P. Organization dependent collective magnetic properties of secondary nanostructures with differential spatial ordering and magnetic easy axis orientation. *Journal of Magnetism and Magnetic Materials,* 408:127, 2016.

(25) Konwar, K., Kaushik, S. D. and Deb, P. Easy axes orientation dependent model for collective magnetic behaviour of zinc ferrite nanoparticles assembly. *AIP Conference Proceedings,* 2265:030548, 2020.

(26) Sharmiladevi, P., Haribabu, V., Girigoswami, K., Farook, A. S. and Girigoswami, A. Effect of mesoporous nano water reservoir on MR relaxivity. *Scientific Reports,* 7:11179, 2017.

(27) Yin, X., Russek, S. E., Zabow, G., Sun, F., Mohapatra, J., Keenan, K. E., Boss, M. A., Zeng, H., Liu, J. P., Viert, A., Liou, S.-H. and Moreland, J. Large T1 contrast enhancement using superparamagnetic nanoparticles in ultra-low field MRI. *Scientific Reports,* 8:11863, 2018.

(28) Carroll, M. R. J., Woodward, R. C., House, M. J., Teoh, W. Y., Amal, R., Hanley, T. L. and St. Pierre, T. G. Experimental validation of proton transverse relaxivity models for superparamagnetic nanoparticle MRI contrast agents. *Nanotechnology,* 21:035103, 2010.

(29) Carr, H. Y. and Purcell, E. M. Effects of diffusion on free precession in nuclear magnetic resonance experiments. *Physical Review*, 94:630, 1954.

(30) Tong, S., Hou, S., Zheng, Z., Zhou, J. and Bao, G. Coating Optimization of Superparamagnetic Iron Oxide Nanoparticles for High T_2 Relaxivity. *Nano Letters,* 10:4607, 2010.

(31) Zhou, Z., Tian, R., Wang, Z., Yang, Z., Liu, Y., Liu, G., Wang, R., Gao, J., Song, J., Nie, L. and Chen, X. Artificial local magnetic field inhomogeneity enhances T_2 relaxivity. *Nature Communications,* 8:15468, 2017.

(32) Zhao, Z., Zhou, Z., Bao, J., Wang, Z., Hu, J., Chi, X., Ni, K., Wang, R., Chen, X., Chen, Z. and Gao, J. Octapod iron oxide nanoparticles as high-performance T_2 contrast agents for magnetic resonance imaging. Nature Communications, 4:2266, 2013.

(33) Nguyen, H. V. T., Chen, Q., Paletta, J. T., Harvey, P., Jiang, Y., Zhang, H., Boska, M. D., Ottaviani, M. F., Jasanoff, A., Rajca, A. andJohnson, J. A. Nitroxide-Based Macromolecular Contrast Agents with Unprecedented Transverse Relaxivity and Stability for Magnetic Resonance Imaging of Tumors. *ACS Central Science,* 3:800, 2017.

(34) Guleria, A., Pranjali, P., Meher, M. K., Chaturvedi, A., Chakraborti, S., Raj, R., Poluri, K. M. and Kumar, D. In vitro and ex vivo relaxometric properties of ethylene glycol coated gadolinium oxide nanoparticles for potential use as contrast agents in magnetic resonance imaging. *Journal of Physical Chemistry C,* 123:18061, 2019.

(35) Zhou, Z., Yang, L., Gao, J. and Chen, X. Structure−Relaxivity Relationships of Magnetic Nanoparticles for Magnetic Resonance Imaging. *Advanced Materials,* 31:e1804567, 2019.